catalysts

MDPI

Article

Acid/Base-Treated Activated Carbon Catalysts for the Low-Temperature Endothermic Cracking of *N*-Dodecane with Applications in Hypersonic Vehicle Heat Management Systems

Kyoung Ho Song [1,2], Soon Kwan Jeong [2], Byung Hun Jeong [3], Kwan-Young Lee [1] and Hak Joo Kim [2,*]

[1] Department of Chemical and Biological Engineering, Korea University, 145 Anam-ro, Seoul 02841, Korea; skh1109@kier.re.kr (K.H.S.); kylee@korea.ac.kr (K.-Y.L.)
[2] Carbon Conversion Research Laboratory, Korea Institute of Energy Research, 152 Gajeong-ro, Yuseong-gu, Daejeon 34129, Korea; jeongsk@kier.re.kr
[3] Agency for Defense Development, Jochiwongil 462, Yuseong-gu, Daejeon 34186, Korea; jeongbh@add.re.kr
* Correspondence: hakjukim@kier.re.kr; Tel.: +82-42-860-3654

Received: 11 August 2020; Accepted: 28 September 2020; Published: 5 October 2020

Abstract: Hypersonic aircrafts suffer from heat management problems caused by the air friction produced at high speeds. The supercritical catalytic cracking of fuel is endothermic and can be exploited to remove heat from the aircraft surfaces using specially designed heat management systems. Here, we report that an acid/base-treated activated carbon (AC) catalyst shows superior performance to the conventional ZSM-5 catalyst at 4 MPa and 450 °C. Further, under these conditions, coke formation is thermodynamically avoided. Of the prepared catalysts, the AC catalyst treated with NaOH and subsequently with HNO_3 (denoted AC-3Na-N) was the most active catalyst, showing the highest selectivity toward light olefins and best heat sink capacity. The acid/base-treated ACs and ZSM-5 catalysts were characterized by scanning transmission electron microscopy, X-ray photoelectron spectroscopy, NH_3 temperature-programmed desorption, and Fourier-transform infrared spectroscopy measurements. Characterization reveals the importance of acid strength and density in promoting the cracking reaction pathway to light olefins observed over the acid/base-treated AC catalysts, which show comparable activity at 450 °C to that of the ZSM-5 catalyst operated above 550 °C. The low-temperature activity suppressed coke and aromatic compound (coke precursors) formation. The stability of the acid/base-treated activated carbon catalysts was confirmed over a time-on-stream of 30 min.

Keywords: activated carbon; acid/base treatment; *n*-dodecane cracking; heat sink; Brønsted acids; Lewis acids

1. Introduction

Hypersonic aircrafts suffer from heat management problems caused by the air friction produced at high speed. At Mach 7, the combustor adiabatic wall temperature has been reported to reach up to 2200 °C, which is beyond the thermal limits of metallic (1200 °C), as well as ceramic (1800 °C), materials [1]. Thus, one of the main challenges facing the commercialization of hypersonic aircrafts is the development of heat management systems specially designed to remove the heat generated by air friction at high speeds. However, strict criteria, such as the heat sink capacity, weight, and operating temperature window, must be observed to preserve the propulsion momentum of the hypersonic engine.

In contrast to heat-insulating ceramics, cooling systems using the endothermic reaction heat derived from the catalytic cracking of liquids have recently received much attention with respect to

expandability and lightness. Specifically, the liquid hydrocarbon fuel used for the hypersonic engine is injected into the channels of a specially designed heat exchanger, and heat control is achieved by absorption of the endothermic heat from cracking and dehydrogenation reactions, as well as by the physical absorption of sensible heat. The gaseous and olefinic products from the cracking reactions are also reported to enhance propulsion efficiency by reducing the ignition delay time [2–7], which is another critical issue in hypersonic engines operating under supercritical conditions.

To date, many researchers have focused on the development of catalytic systems based on acid catalysts, such as ZSM-5 zeolite and composite oxide catalysts, which are mostly active above 550 °C [8–14]. However, the conventional ZSM-5 zeolite catalyst, which has abundant Brønsted acid sites and is active above 550 °C, is easily deactivated by coke deposition, which results in the blockage of the microporous structure [15]. On the other hand, composite oxide catalysts could be resistant to coke deposition because of the lower acid density than that of the ZSM-5 zeolite, although this results in lower activity and poor heat sink capacity, even at high temperatures [16].

The reaction mechanism of hydrocarbon cracking over heterogeneous solid acid catalysts has been well defined [17–23]. The catalytic cracking of *n*-paraffins is generally accepted to be a multistep process, as illustrated in Scheme 1. The protolytic cracking proceeds via a penta-coordinated alkanium ion formed by the protonation of paraffin at the Brønsted acidic site (step 1). The transition state alkanium ion is decomposed to form hydrogen or light paraffins (mainly CH_4 and C_2H_6) and a smaller carbenium ion (step 2). Subsequently, the carbenium ion yields olefins, giving back the proton to the catalyst to regenerate the Brønsted acid sites (reverse step 5) or proceeds to β-scission to produce light olefins and smaller carbenium ions (step 3). Carbenium ions can also be generated by hydride abstraction from paraffins on Lewis acid sites (step 4) and by the protonation of olefins over Brønsted acid sites (step 5).

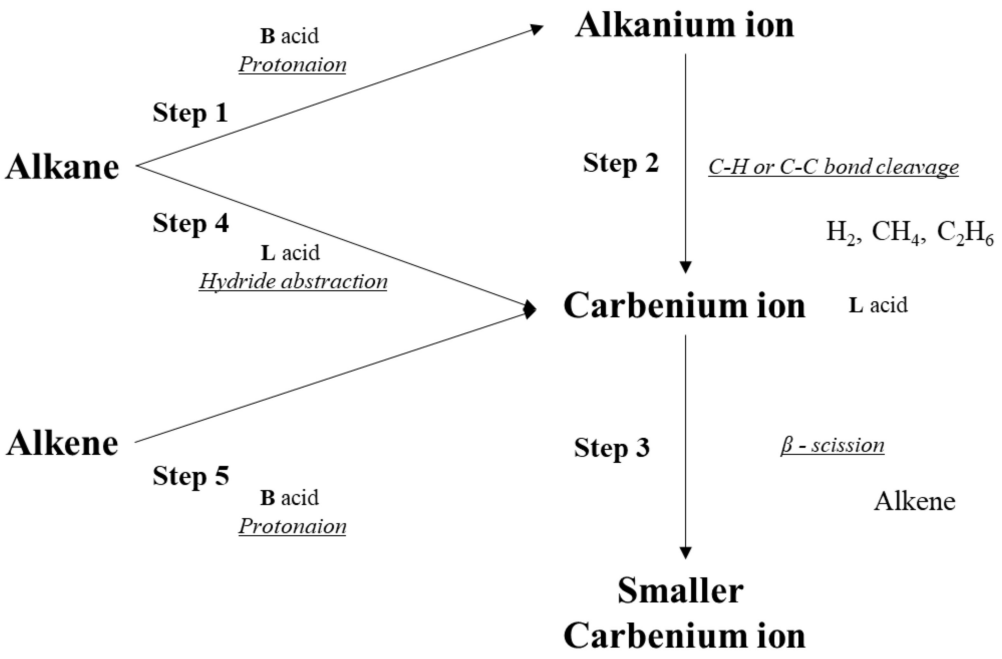

Scheme 1. Cracking reaction mechanism over heterogeneous solid acid catalysts.

Interestingly, hydrogen and light paraffins, such as methane and ethane, are only produced from the decomposition of alkanium ions to carbenium ions (step 2), and only paraffins are generated by β-scission. Crucially, the product's distribution depends on the number and type of reactions, which is dictated by the type of acid catalyst, as well as the acid site strength and density. Wojciechowshi et al. [18,19] suggested that differences in the speed of interionic reactions depending

on the acid strength and properties of the solid heterogeneous catalyst affect product selectivity and coke formation during *n*-paraffin cracking.

Activated carbon (AC) is frequently used in many industrial applications because of its large specific surface area, easy control over the pore structure by simple physicochemical treatment, and cost competitiveness for mass production. A large amount of AC is used to remove the organic impurities contained in electroplating solutions for metal finishing. It is also widely employed in environmental processes, such as drinking water filtration, volatile organic compound (VOC) capture, mercury scrubbing from coal-fired power plants, and air purification [24–31]. ACs are generally produced by carbonization at temperatures in the range of 600–900 °C in an inert atmosphere from source materials such as bamboo, coconut husk, wood, coal, and willow peat. The activation process is carried out by exposing the carbonized material to mild oxidizing conditions between 600 and 1200 °C [32]. Chemical activation is achieved by subjecting the carbon materials to chemicals such as acids, bases, or salts at 250–600 °C. Chemical activation resulted in the formation of a microscopic pore structure with high surface area. Furthermore, acid treatment also generates surface acidity because of the addition of surface oxygen functional groups (OFGs), such as phenolic hydroxyl (C-OH, -C-O-), carboxylic (-COOH), and carbonyl (C=O) OFGs [32–38], as shown in Figure 1.

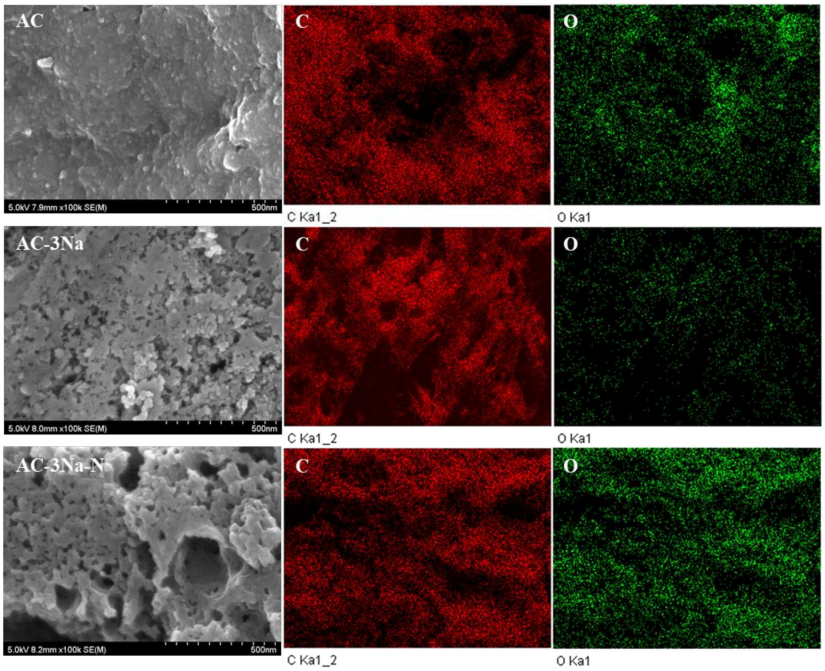

Figure 1. SEM surface texture and EDX elemental maps of AC, AC-3Na, and AC-3Na-N catalysts.

On the other hand, base treatment with KOH or NaOH generates both micro- and meso-porous structures by the formation of defects from the redox reactions of hydroxide and carbon skeleton. The hydroxide reduction results in the formation of H_2 and Na or K metal and carbon is oxidized to metal carbonates according to the reaction shown in Equation (1). The metal carbonates further oxidize the carbon skeleton or are decomposed to metal oxides, producing gaseous CO_2 and CO (Equations (2) and (3)). The metal oxides can be removed from the surface by washing [39–41].

$$6NaOH + 2C \rightarrow 2Na + 3H_2 + 2Na_2CO_3 \quad (1)$$

$$Na_2CO_3 + C \rightarrow Na_2O + 2CO_2 \quad (2)$$

$$Na_2CO_3 \rightarrow Na_2O + CO \quad (3)$$

$$2Na + CO_2 \rightarrow Na_2O + CO \quad (4)$$

In this work, acid/base-treated AC catalysts were applied to the supercritical catalytic cracking of *n*-dodecane for the heat management of hypersonic vehicles operating at speeds greater than Mach 7. To maximize the generation of surface OFGs, the sequence of the acid and base treatments was optimized. An initial base treatment was found to be effective to build defects and a micro- and meso-porous structure. Consecutive acid treatment mainly generated carboxylic (-COOH) OFGs, yielding an acidic surface structure in the AC catalyst. Catalyst characterization using X-ray photoelectron spectroscopy (XPS), ammonia temperature-programmed desorption (NH_3-TPD), and Fourier transform infrared (FT-IR) spectroscopy were used to identify the OFGs, to quantify the acid type, strength, and density, and quantify the activity and selectivity of the catalysts based on the reaction mechanism. This is the first report of an AC catalyst being treated first with NaOH and further with HNO_3 (AC-3Na-N). Crucially, the catalyst had comparable activity at 450 °C to that of the ZSM-5 catalyst operated above 550 °C (see Table S5). The low-temperature activity suppressed the formation of coke and aromatic compounds known to be coke precursors. The stability of the acid/base-treated AC catalysts was confirmed over a time-on-stream of 1 h.

2. Results

The prepared AC catalysts are labeled based on the sequence of the base (-Na) and acid (-N) treatment process, where the number preceding (-Na) denotes the NaOH/AC weight fraction. As an example, the AC-3Na-N catalyst represents the AC catalyst treated first with NaOH at a NaOH/AC weight fraction of 3 subsequently treated with HNO_3. The bare AC and ZSM-5 catalysts are labeled AC and ZSM-5, respectively.

2.1. Physical Properties of the AC Catalysts

The N_2 adsorption–desorption isotherms of the ACs and ZSM-5 zeolite catalysts are shown in Figure S2a. Type IV behavior was observed for all catalysts. The characteristics of a microporous structure can be observed in the range of 0 to 0.47 atm, and the presence of mesoporous structure is indicated by the hysteresis loops between 0.47 and 1 atm. The pore size distributions calculated by the Barrett–Joyner–Halenda method are shown in Figure S2b. The average pore diameter was between 3 and 4 nm for all the AC catalysts, but the AC-3Na-N catalyst was observed to have additional large pores (4 to 8 nm, see Figure S2). On the other hand, the ZSM-5 zeolite catalyst had an average pore size of 2.5 nm, which indicates the presence of a dominant microporous structure. The physical properties of the ACs and ZSM-5 zeolite catalysts are summarized in Table 1. The acid (HNO_3)-treated AC-N and AC-3Na-N catalysts showed a 5% decrease in specific surface area and 30% decrease in pore volume compared with AC and AC-3Na catalysts, respectively. On the basis of previous studies of the nitric acid treatment of AC, this phenomenon can be explained by the fact that the newly formed OFGs might distort the initial flat carbon layers, blocking the original pores between layers [42,43]. In contrast, the base-treated AC-1Na and AC-3Na catalysts showed increases in both the micro- and mesopore surface area. Notably, the specific surface area and pore volume of the AC-3Na catalyst increased by 2.3 and 2.2 times, respectively, compared with that of the bare AC catalyst. As discussed, additional mesopores might have been generated by the formation of defects when the carbon framework was eroded by the reduction in NaOH [39–41].

2.2. Surface Texture and EDX Elemental Mapping SEM Images of the AC Catalysts

The scanning electron microscopy (SEM) surface texture and energy dispersive X-ray (EDX) elemental maps' images of the AC, AC-3Na, and AC-3Na-N catalysts are shown in Figure 1. The EDX and XPS determined surface compositions are summarized in Table S1. As shown by the SEM images, the base-treated AC-3Na and AC-3Na-N catalysts showed additional development of a porous structure compared with that of the bare AC catalyst. The effect of nitric acid treatment is clearly shown by the increased intensity and distribution of the formed OFGs, as shown in the EDX map for oxygen in the AC-3Na-N catalyst (Figure 1).

Table 1. Physical properties of fresh AC and ZSM-5 zeolite catalysts.

Sample	S_{BET} [a]	Micropore S.A [b]	Mesopore S.A [c]	V_{total} [d]	V_{micro} [e]	V_{meso} [f]	P [g]
	($m^2 \cdot g_{-cat}^{-1}$)			($cm^3 \cdot g_{-cat}^{-1}$)			(nm)
AC	565	321	244	0.41	0.17	0.24	4.7
AC-N	538	299	239	0.39	0.16	0.23	4.6
AC-1Na	670	374	296	0.47	0.20	0.27	4.4
AC-3Na	1315	673	642	0.88	0.35	0.53	4.0
AC-3Na-N	983	460	523	0.63	0.24	0.39	3.5
ZSM-5	294	248	46	0.18	0.12	0.06	2.5

[a] Brunauer-Emmett-Teller (BET) surface area (S.A.); [b] Microporous surface area, Microporous S.A = S_{BET} − t-plot; [c] Mesopore surface area, Mesopore S.A = S_{BET} − Micropore S.A; [d] Total volume adsorbed at P/P_0 = 0.99; [e] Micropore volume (r < 2 nm); [f] Mesopore volume, $V_{meso} = V_{total} - V_{micro}$; [g] Average pore diameter.

As mentioned in the introduction, the formation of OFGs by acid treatment with nitric acid can proceed by two reactions, as illustrated in Scheme 2. Because carbon atoms have excellent stability in the condensed aromatic structure, OFGs are likely to be formed on defect sites with sp^3 hybridized carbon atoms, known as aliphatic side chain carbons [44]. The dicarboxylic acid OFG can be formed by the C-C bond cleavage of aliphatic side chains. Ketone OFGs can be generated on aliphatic side chains containing methylene groups, which is similar to the oxidation of diphenylmethane [35,36]. The sequential treatment of base and acid was found to be effective to induce the formation of abundant OFGs. The resultant enlargement in surface area, as well as defect sites with base treatment, increased the number of OFGs by 22.5 at.%, as confirmed by EDX elemental composition analysis.

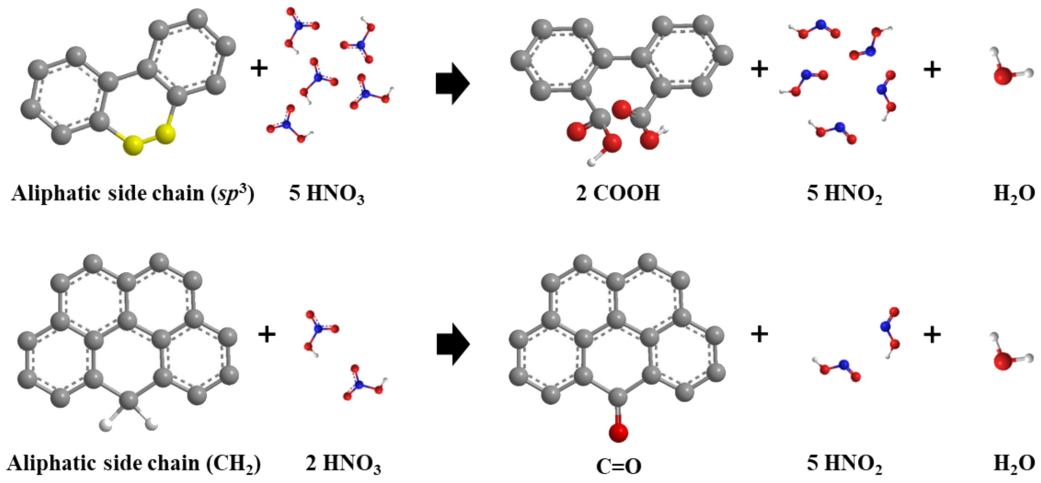

Scheme 2. Oxygen functional group generation on Activated carbon (AC) after HNO_3 acid treatment (adapted from [35,36]).

2.3. XRD Analysis of the ACs and ZSM-5 Zeolite

Figure S3 presents the X-ray diffraction (XRD) patterns of the AC and ZSM-5 zeolite catalysts. The XRD pattern of the ZSM-5 catalyst is consistent with that of the typical H-ZSM-5 (JCPDS 44-0003). For the AC catalysts, broad peaks with low intensity were observed at 23° and 43°, and these are characteristic peaks of the (002) and (101), respectively, crystal faces of ACs. The lattice layer spacing (d_{002}) and crystallite size were calculated using the (002) face, and the values are summarized in Table S2.

The acid treatment was found to reduce the lattice layer spacing with apparent decrease in crystallite size, whereas the base treatment showed completely the opposite phenomenon. The base treatment might enlarge the lattice layer spacing by the formation of defect sites from the decay of the framework carbon atoms in the condensed aromatic structure [32]. In contrast, acid treatment is

believed to narrow the layer spacing by the formation of bent OFGs in the sp^3 hybridized carbon atoms rather than the flat sp^2 structure. The formation of sodium metal, oxides, and salts was not detected.

2.4. XPS Analysis of AC Catalysts

The wide-scan XPS scans of the five catalysts are shown in Figure S4. The atomic elemental compositions calculated from the relative sensitivity factors and spectral areas are also summarized in Table S1. The narrow-scan XPS spectra of C1s and O1s are presented in Figure S5 and Figure 2, respectively, and were used to understand the identity and composition of the surface FGs using the deconvolution technique.

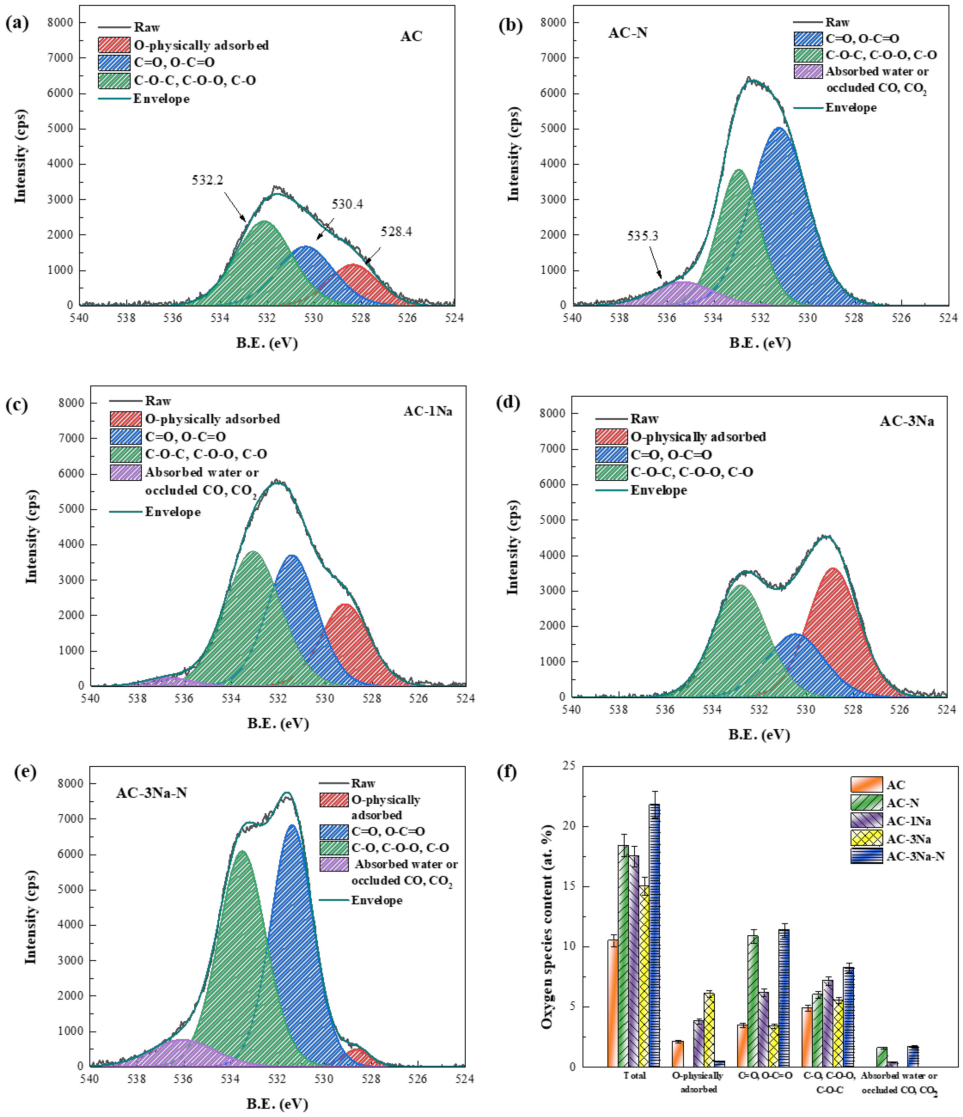

Figure 2. Deconvolution of the XPS O1s spectra of the AC catalysts: (**a**) AC, (**b**) AC-N, (**c**) AC-1Na, (**d**) AC-3Na, (**e**) AC-3Na-N, and (**f**) oxygen species content (B.E. = binding energy).

The deconvolution of the C1s spectra of the AC catalysts yielded a main peak at 284.8 eV, which can be assigned to the graphitic sp^2 carbon structure [44]. Furthermore, the peak centered at 285.7 eV can be attributed to the aliphatic sp^3 carbon structure present at defect sites [44], whereas those located at 286.7, 288.5, and 290.0 eV correspond to carbon atoms bound to one, two, and three oxygen atoms, respectively [45,46]. Finally, the peak observed at 292.1 eV can be assigned to the π–π^* transition loss peak. Based on the deconvolution of the O1s spectra between 529 and 536 eV, four different types of

OFGs were identified. The peak at 529 eV can be attributed to the bulk oxygen physically adsorbed on carbon, whereas that at 531 eV was attributed to the oxygen double bonded to carbon. The peak at 533 eV was assigned to the oxygen linked to carbon by a single bond, and that at 536 eV was assigned to oxygen from adsorbed water molecules [44].

From the quantitative analysis of the carbon species content by XPS shown in Figure S5f, AC was found to contain 56.0 at.% of sp^2 carbon species, which represents the most stable carbon structure in the AC catalysts. The base treatment with NaOH was found to convert the sp^2 carbon species of the stable framework to sp^3 carbon species, thus forming a defective structure. In particular, in the case of AC-3Na, of the AC catalysts, the content of sp^3 carbon species reached the highest value of 16.2 at.%.

From the quantitative analysis of the oxygen species content by XPS shown in Figure 2f, the AC-N and AC-3Na-N catalysts treated with HNO_3 acid showed significant increase in the total oxygen content (7.9 and 11.3 at.%, respectively) compared to that of the bare AC catalyst, mainly by the formation of doubly (C=O) and triply (O-C=O) oxygen-bound carbon. Interestingly, base-treated AC-1Na and AC-3Na catalysts were also observed to have increased total surface oxygen contents (7.0 and 4.5 at.%, respectively) compared to that of the AC catalyst, respectively. Defect sites with uncoordinated sp^3 hybridized carbon atoms might have been formed after the base treatment. Subsequently, the surface oxidation of the uncoordinated sp^3 hybridized carbon atoms would have proceeded to generate OFGs in a similar way to the activation process by physical treatment reported in our previous work [47]. Therefore, it is difficult to interpret the results of the quantitative analysis of OFGs derived from the base treatment alone.

2.5. FT-IR Analysis of AC Catalysts

To identify the surface FGs present on ACs before and after the acid/base treatment, FT-IR analysis was performed in absorbance mode. Because it was difficult to discriminate the differences in the intrinsic sensitivity between samples, only a qualitative assignment of absorbance bands at different wavenumbers was conducted to differentiate the surface FGs present on the surface of the ACs. Additionally, the intensity of the peak corresponding to adsorbed gaseous CO_2 at 2349 cm^{-1} was too strong to provide any useful information. Thus, the absorbance band data from 2400 to 1900 cm^{-1} are omitted in Figure 3. A broad band between 3663 and 3002 cm^{-1} was observed in the spectra of all ACs and can be attributed to the stretching O-H vibrations of hydroxyl groups and physically absorbed water [48–50]. The characteristic bands of O-H stretching from carboxylic (3500 cm^{-1}) and phenolic (3605–3393 cm^{-1}) FGs are present and overlapped between 3663 and 3002 cm^{-1} [51]. The two bands located at 2916 and 2844 cm^{-1} are assigned to C-H symmetrical and asymmetric stretches of methylene (-CH_2-) FG, respectively [52]. In general, the typical absorption bands of OFGs present on ACs were observed between 2000 and 1000 cm^{-1}. The band located at 1710 cm^{-1} was assigned to the C=O stretches of carboxylic acids (COOH) FG [53] and the band at 1571 cm^{-1} to that of the ketone FG [53,54]. The band located at 1128 cm^{-1} was attributed to O-H stretching of the phenolic FGs [55]. The absorption bands corresponding to carboxylic, ketone, and phenolic OFGs were observed on the acid-treated AC-N and AC-3Na-N catalysts. In contrast to the bands in the spectra of the AC and AC-3Na catalysts, sharp absorption bands of carboxylic OFG can be clearly seen in the spectra of the AC-N and AC-3Na-N catalysts, indicating the introduction of OFGs with acid treatment. In particular, for the AC-3Na catalyst, the relative intensity of the absorption band of OFGs was definitely broadened because of the abundance of OFGs by sequential treatment with base and acid.

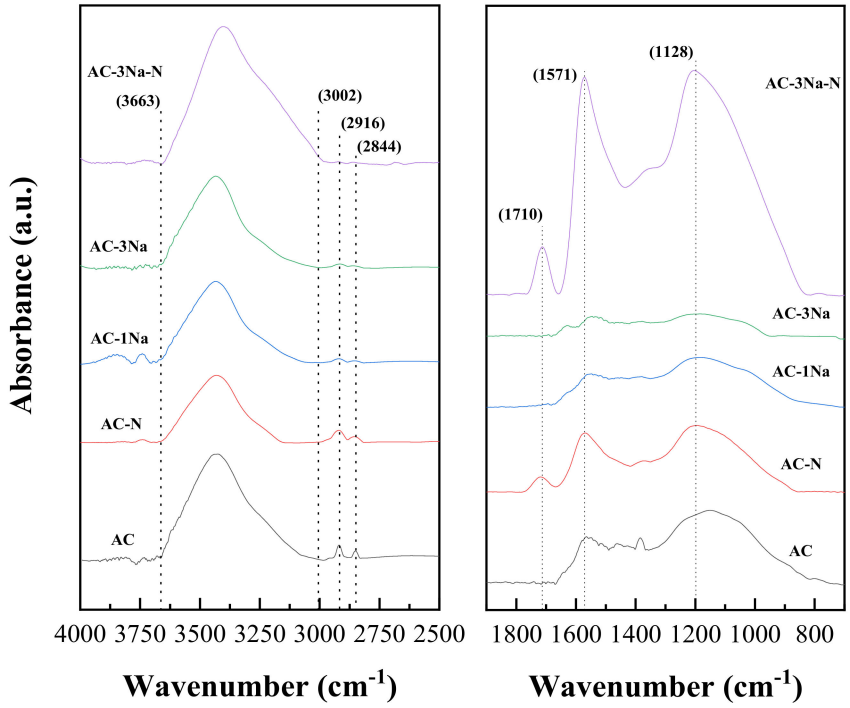

Figure 3. FT-IR spectra of AC catalysts.

2.6. Acid Properties of AC and ZSM-5 Zeolite Catalysts

Investigation of solid aluminosilicate catalysts has shown that the catalytic activity and product selectivity for the cracking of hydrocarbons are related to the type of solid acid catalyst [18,19]. The XPS and FT-IR analyses confirmed that sequential treatment of base and acid was effective in generating OFGs on the AC defect sites. In particular, the carboxylic FG might function as an acidic site that can catalyze the cracking reaction. For the quantitative measurement of acid properties of the catalysts, NH_3-TPD analysis was performed and the results are presented in Figure 4. From the NH_3-TPD profiles, three types of acid strength were assigned depending on the desorption temperature: weak (α sites: 50–250 °C), medium (β sites: 250–490 °C), and strong acid sites (γ sites: 490–720 °C). The differentiation between Brønsted (B) and Lewis (L) acid can be easily made using NH_3 in situ FT-IR analysis. Absorption bands at 1440–1470 and 1610–1640 cm^{-1} are characteristic of B and L acid sites, respectively [56–59]. The acid site densities (ASD) and B/L acid ratio were calculated from the quantitative analysis of NH_3-TPD and NH_3 in situ FT-IR (Figure 5), and the values are summarized in Table 2. Assuming that the NH_3 adsorption sites for FT-IR spectroscopy and TPD analysis are identical, the B and L ASDs were calculated by multiplying the total ASD by $\left(\frac{B/L}{B/L+1}\right)$ or $\left(\frac{1}{B/L+1}\right)$, respectively [60].

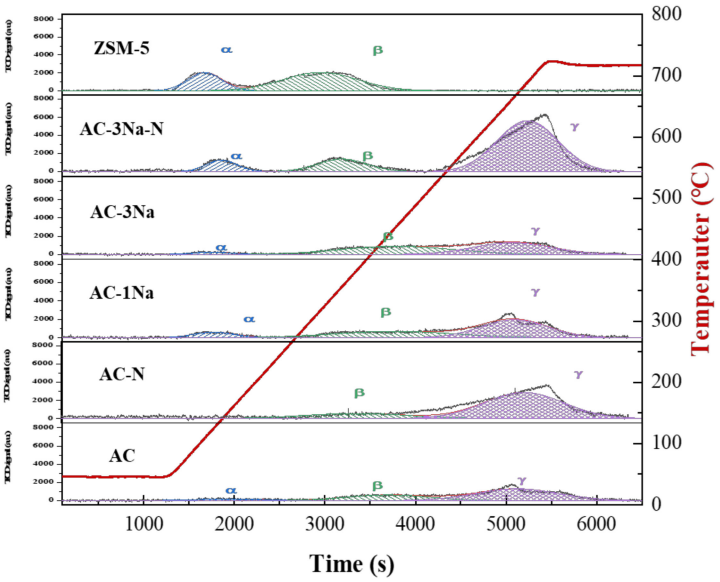

Figure 4. NH_3- temperature programmed desorption (TPD) profiles of fresh ACs and ZSM-5 zeolite.

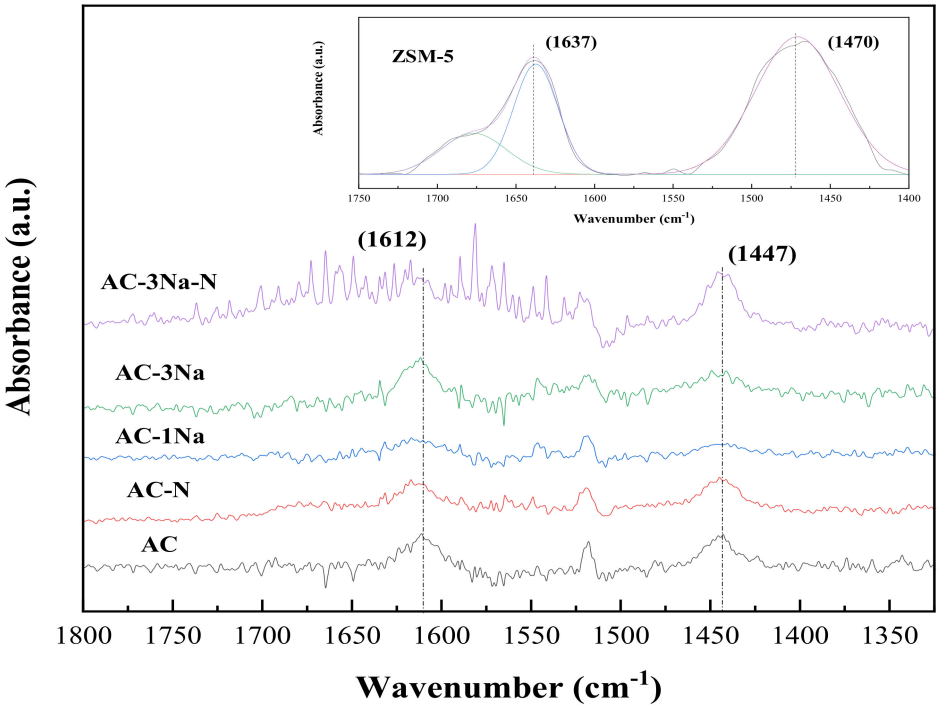

Figure 5. In situ NH_3-desorption FT-IR spectra of ACs and ZSM-5 zeolite.

Table 2. Acid site densities of ACs and ZSM-5 zeolite.

Sample	Acid Site Density				B/L ASD Ratio [b]	Acid Site Density	
	Weak (α)	Medium (β)	Strong (γ)	Total [a]		Brønsted [c]	Lewis [c]
	(mmol-NH_3/g-$_{cat}$)					(mmol-NH_3/g-$_{cat}$)	
AC	0.061 (7.1%)	0.258 (30.0%)	0.54 (62.9%)	0.859	0.99	0.43	0.43
AC-N	0 (0%)	0.376 (20.3%)	1.473 (79.7%)	1.849	1.30	1.04	0.81
AC-1Na	0.138 (10.3%)	0.468 (35.0%)	0.733 (54.7%)	1.339	0.52	0.46	0.88
AC-3Na	0.057 (4.7%)	0.574 (47.8%)	0.571 (47.5%)	1.202	0.74	0.51	0.69
AC-3Na-N	0.239 (8.8%)	0.418 (15.3%)	2.071 (75.9%)	2.728	3.16	2.07	0.66
ZSM-5	0.511 (52.6%)	0.461 (47.4%)	0 (0%)	0.972	2.36	0.58	0.39

[a] The acid site densities were obtained by integrating the NH_3-TPD curves shown in Figure 4. [b] B/L ratios were calculated by the in situ NH_3 desorption FT-IR spectroscopy results shown in Figure 4. [c] Numbers of Brønsted and Lewis acid were calculated using total acid amount and B/L ratio.

From the results of NH_3-TPD analysis, the total acid site density present on catalysts decreased in the following order: AC-3Na-N > AC-N > AC-1Na > AC-3Na > ZSM-5 > AC. This result shows that the acid and base treatment increased the acidity of the AC catalysts. In particular, the AC-3Na-N catalyst sequentially treated with base and acid showed a significant increase in strong γ acid sites: up to 2.071 mmol-NH_3/g-cat. In our previous study, carboxylic OFGs were found to produce strong acidity on physically treated AC catalysts [43]. In accordance with XPS and FT-IR analysis results, the sequential base and acid treatment led to the formation of many carboxylic acid OFGs, as shown by the increase in the strong ASD by the formation of Brønsted acid sites. On the other hand, Lewis acid sites are thought to form at defect structures with sp^3 hybridized unsaturated carbon atoms, which could accept a pair of nonbonding electrons. Thus, it can be concluded that the base treatment generated Lewis acid sites by the formation of undercoordinated sp^3 hybridized carbon atoms. The base-treated AC-1Na and AC-3Na catalysts were found to have a larger amount of Lewis ASD compared with acid-treated AC-N and AC-3Na-N catalysts.

2.7. Cracking Activity

The thermal and catalytic cracking of *n*-dodecane were assessed at 4 MPa and 450 °C over the AC and ZSM-5 catalysts. The results are shown in Figure 6. The use of the catalysts clearly improved the liquid fuel conversion, as well as gas yield and heat sink capacity. Among the tested catalysts, the AC-3Na-N catalyst showed the highest liquid fuel conversion of 77.4%, which decreased in the following order: AC-3Na-N (77.4%) > AC-N (63.6%) > AC-1Na (59.2%) > AC-3Na (55%) > ZSM-5 (48.3%) > AC (45.5%) > thermal cracking (26.9%). The liquid fuel conversion order between catalysts was in complete coincidence with their order of total ASD. Therefore, we suggest that all the acid sites present on the catalyst surface were involved in the conversion of *n*-dodecane. Similarly, the gas production yield showed to decrease in the order of AC-3Na-N (61.1%) > AC-N (45.3%) > AC-1Na (39.9%) > AC-3Na (37.7%) > AC (26.9%) > ZSM-5 (24.3%) > thermal cracking.

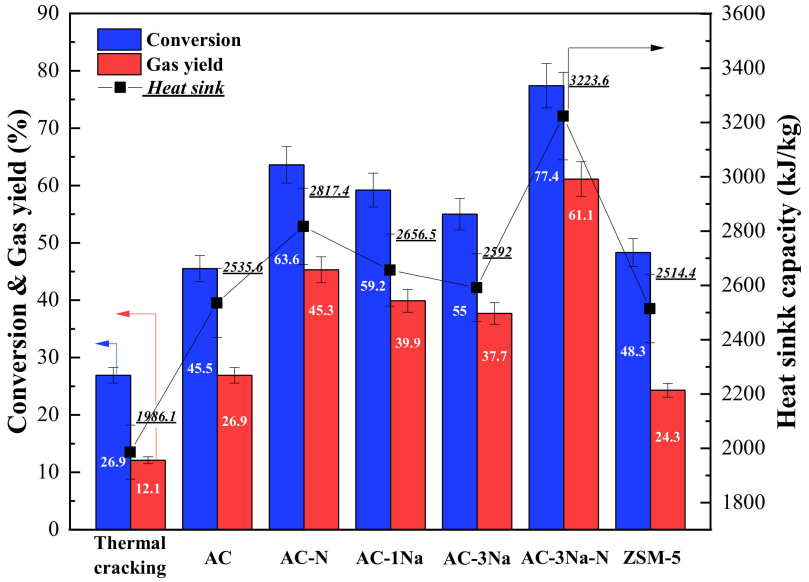

Figure 6. Conversion, gas production yield, and heat sink capacity at 450 °C and 4 MPa.

The heat sink capacity was found to decrease in the order of AC-3Na-N (3223.6 kJ/kg) > AC-N (2817.4 kJ/kg) > AC-1Na (2656.5 kJ/kg) > AC-3Na (2592 kJ/kg) > AC (2535.6 kJ/kg) > ZSM-5 (2514.4 kJ/kg) > thermal cracking (1986.1 kJ/kg), in the same manner as the strong ASD and gas production yield.

Figure 7 shows the gaseous product distribution and olefin-to-paraffin ratios based on the cracking reaction of *n*-dodecane carried out at 450 °C and 4 MPa. The main gaseous products were methane, ethane, ethene, propane, propene, *n*-butane, and 1-butene. The olefin-to-paraffin ratios of the gaseous products (O/L ratio) were all higher than 1, except for the ZSM-5 zeolite catalyst. In particular, the AC-N catalyst showed the highest O/L ratio of 1.32.

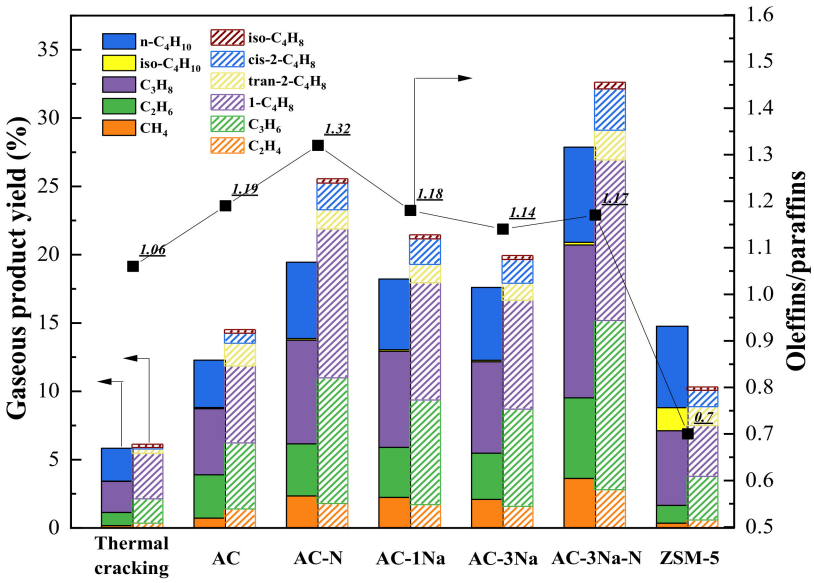

Figure 7. Gaseous product yield at 450 °C and 4 MPa.

The overall product distribution is illustrated in Figure 8 and Table S4. Paraffins, C_2–C_4 olefins, C_5–C_{12} olefins, aromatics, and naphthenes were the main products. Overall, the treated AC catalysts showed higher product selectivity toward olefins than the ZSM-5 and AC catalysts and thermal cracking,

which exceeded 72% of product selectivity to paraffins. Catalysts with strong ASDs, such as AC-3Na-N and AC-N catalysts, tended to produce larger amount of gaseous C_2–C_4 olefins. In particular, AC-3Na-N showed the highest gaseous olefin product selectivity of 32.7%. Interestingly, ZSM-5 catalyst exhibited considerable production of aromatics and naphthalenes, which are well-known coke precursors.

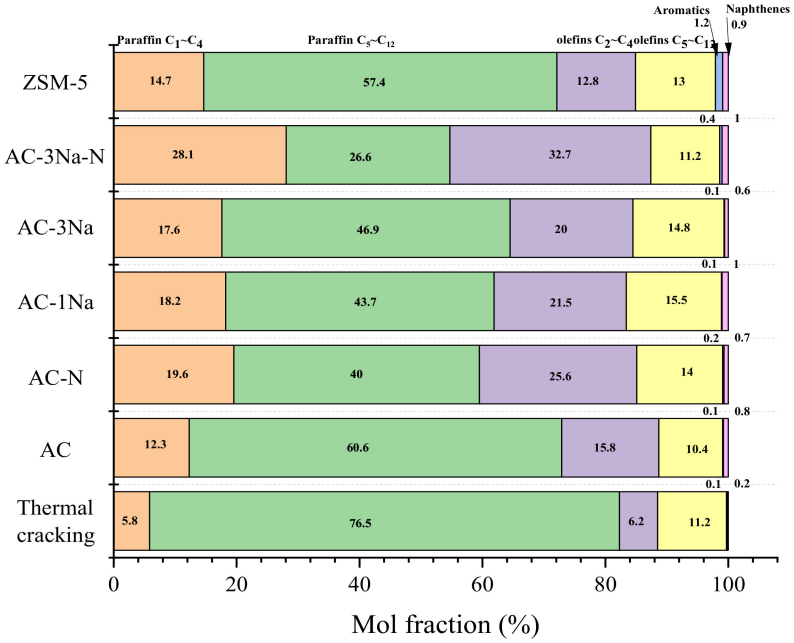

Figure 8. Overall product distribution at 450 °C and 4 MPa.

3. Discussion

From the results of XPS, FT-IR, and NH_3-TPD analysis, it can be concluded that base treatment of AC resulted in the formation of unsaturated sp^3 hybridized carbon sites, which might act as acceptors of nonbonded ion pairs and, thus, act as Lewis acid sites. The acid treatment of AC gave rise to the formation OFGs such as carboxylic acids (COOH), which might act as Brønsted acid sites. Moreover, the sequential base and acid treatment on AC was effective in generating both Brønsted and Lewis acid sites with strong acidity, as well as a large ASD. As mentioned in the previous section, the initial step of *n*-dodecane cracking involves the formation of penta-coordinated alkanium ion at the Brønsted acidic site. The alkanium ion is decomposed into a smaller carbenium ion producing light paraffins such as methane, ethane, or hydrogen. Considering the overall reaction mechanism, light paraffins are mainly produced during the above step. The produced carbenium ion is further decomposed to much smaller carbenium ion, thus producing olefins via β-scission. Olefins can be further decomposed to smaller olefins via step 5 in Scheme 1 on Brønsted acid sites or rearranged to form cyclic and aromatic compounds. Cyclic and aromatic compounds can further react, polymerize, and form coke, and it has been reported that the steric blockage of the formed aromatic compounds within the micropores facilitates the formation of coke [61]. Even though the catalytic cracking was carried out at a relatively low temperature of 450 °C, the formation of aromatic compounds was noticeable within the ZSM-5 zeolite catalyst, as shown in Figure 8. This phenomenon can be explained by the fact that the ZSM-5 zeolite catalyst contains mainly micropores with Brønsted acid sites; thus, the produced olefins might further react to form aromatic compounds within the blocked micropores. The formation of coke is widely reported to occur at 550–600 °C over the ZSM-5 zeolite catalyst [10]. In our present study, the cracking reaction was carried out at 450 °C, which seemed to retard coke formation within the micropores of ZSM-5. The catalytic activity of ZSM-5 catalyst on *n*-dodecane reported in the literature is summarized in Table S5. It seems reasonable that the liquid fuel conversion reached above 70% when the reaction temperature was increased up to 550–600 °C, at which coke formation was inevitable.

The main advantage of the AC catalysts is that they were active at lower reaction temperature (450 °C) than the ZSM-5 catalyst, and coke formation was thermodynamically suppressed, even at a high liquid fuel conversion level of 70%. Furthermore, the mesoporous structure of ACs might enhance the mass transfer within the pores, which would restrain the further reaction of olefins to form aromatic compounds. AC catalysts showed aromatic and naphthalene product selectivities of less than 1%. However, in the case of AC-3Na-N, the abundance in the Brønsted acidic site is believed to generate non-negligible amounts of aromatic compounds.

In addition to the type of acid (Brønsted and Lewis acid), the acid strength, as well as ASD, should also be considered to account for the product distribution and yield. Strong acid sites might lead to the formation of more stable carbenium ions with increased turnover number on the catalyst surface, thus intensifying β-scission reactions. Furthermore, a higher ASD would have direct effect on the number of active sites present on the surface of catalyst for the conversion of liquid fuel. By all accounts, the catalytic cracking of *n*-dodecane should be understood in-depth based on the type, strength, and acid density of the acid catalysts. From the cracking activity results presented in Figures 6–8, two strong correlations were observed. First, the liquid fuel conversion and gaseous paraffin (C_1-C_4) yield showed proportional relationship with total ASD in the following order: AC-3Na-N > AC-N > AC-1Na > AC-3Na > ZSM-5 > AC > thermal cracking, whereas the liquid paraffin (C_5-C_{12}) yield showed the reverse trend. Second, the overall gaseous product yield, gaseous olefin (C_1-C_4) yield, and heat sink capacity matched the order of strong ASD: AC-3Na-N > AC-N > AC-1Na > AC-3Na > AC > ZSM-5 > thermal cracking. These two correlations are similar with the exception of the AC and ZSM-5 catalysts. The gas production yield of the bare AC catalyst exceeded that of ZSM-5 despite the lower liquid fuel conversion level. Strong acidic sites are reported to result in C-C bond cleavage from normal paraffin to produce gaseous products such as methane, ethane, and hydrogen by the formation of alkanium ions in the initial stages of the cracking reaction, as illustrated in Scheme 1. Even though the ZSM-5 catalyst had a greater ASD than the bare AC catalyst, it showed lower gas production yield because of the deficiency of the strong acidic site. The bare AC catalyst used in this work was commercial grade, and activation was carried out via mild oxidative treatment. As shown in our previous work, physical treatment at high temperatures (up to 400 °C) under mild oxidizing conditions is effective in generating OFGs with strong acidity. Thus, the high ASD of 0.54 mmol-NH_3/g-cat was determined to be due to the initial OFGs present in the bare AC catalyst.

4. Materials and Methods

4.1. Materials

ZSM-5 zeolite (SiO_2/Al_2O_3 molar ratio = 23) was purchased from Zeolyst (Zeolyst Co., Kansas, KS, USA). The granular type AC was purchased from Sigma-Aldrich (Sigma-Aldrich Co., St. Louis, MO, USA). Before use, particles between 30 and 50 mesh were selected. HNO_3 (analytical grade, 70%) and NaOH (analytical grade, ≥98%) were used as purchased from Sigma-Aldrich without any further purification.

4.2. Catalyst Synthesis

Base treatment with NaOH was employed as follows: AC was mixed with a 2 g and 6 g NaOH. The mixed sample was heated from room temperature to 850 °C at a heating rate of 10 °C/min and was maintained at 850 °C for 3 h under an argon atmosphere to prevent surface oxidation. The collected solid sample was washed with 0.1 M nitric acid solution and deionized (DI) water until the filtrate reached a pH of 7. The obtained solid was dehydrated at 100 °C overnight in an oven. The amount of NaOH used in the treatment was varied from a NaOH/AC weight fraction of 1 to 3.

Acid treatment with HNO_3 was carried out by adding 2 g of fresh AC to 60 mL of 70% HNO_3 to a 500-mL single-necked round-bottomed flask fitted with a simple reflux system. Aging was

undertaken at 60 °C for 16 h. The slurry was filtered and rinsed repeatedly with DI water until the filtrate reached a pH of 7. The obtained solid was dried overnight at 100 °C in an oven.

4.3. Catalytic Activity Evaluation

As shown in Figure S1, the catalytic cracking of *n*-dodecane was carried out under supercritical reaction conditions using a fixed-bed reactor. *n*-dodecane was supplied to a stainless-steel tube reactor (SUS-316L, O.D. 1/4 in., thickness 0.89 mm, length 310 mm) at 0.2 mL/min using a high-performance liquid chromatography (HPLC) pump (YL9200N, Young Lin Instrument Co., Anyang, Gyeonggi-do, South Korea), where 0.1 g of catalyst was fixed with the aid of quartz wool. The reactor temperature was increased using an electric heater and a proportional–integral–derivative (PID) controller. The power consumption of the electric heater was monitored to determine the heat sink capacity. The reaction was carried out at 450 °C and 4 MPa using a back-pressure regulator (TESCOM Co., Pflugerville, TX, USA). The product gas and liquid were cooled at the condenser and then, separated in liquid collector. The volume of the gaseous products was measured using a wet gas meter (W-NKDa-1B, Shinagawa Co., Inagi-shi, Tokyo, Japan) and then, collected in gas-tight bags (TEDLA (CEL Scientific Co., Cerritos, CA, USA), 10 L). The collected C_5–C_{12} liquid hydrocarbons were analyzed with an offline gas chromatography (GC) system (Agilent 7890B, Agilent Co., Santa Clara, CA, USA) using the detailed hydrocarbon analysis (Detailed Hydrocarbon Analyzer (DHA), ASTM D6730) method [62]. The C_1–C_4 gaseous products were analyzed by GC (6500YL, Young Lin Instrument Co., Anyang, Gyeonggi-do, South Korea) using a flame ionization detector (FID) and GS-GasPro capillary column (30 m × 0.32 mm). Detailed GC analysis conditions were summarized in Tables S6 and S7. The conversion of *n*-dodecane, the product selectivity, and the heat sink capacity were calculated using Equations (5)–(7) after 20 min, at which steady-state was reached and sustained within 1 h on stream. The products analysis was conducted with the samples collected within 10 min after steady-state conditions were reached.

$$\text{Coversion (X)} = \left(\frac{\text{Initial moles of linear dodecane} - \text{ Final moles of linear dodecane}}{\text{Initial moles of linear dodecane}}\right) \times 100\% \quad (5)$$

$$\text{Selectivity (S)} = \left(\frac{\text{Moles of each product}}{\text{Moles of total products}}\right) \times 100\% \quad (6)$$

$$\text{Heat sink capacity (Q)} = \frac{\text{Electrical power(kW)} \times \text{Thermal efficiency}(\eta)}{\text{Mass flow rate of linear dodecane (kg/s)}} \quad (7)$$

The power consumption of the electrical heater was measured during catalytic cracking to maintain isothermal reaction conditions at 450 °C. The heat loss to the environment is reflected by the thermal efficiency, η. The power consumption during heating from room temperature (RT) to 450 °C with N_2 flow was measured, and η was calculated as the ratio of the ideal sensible heat of N_2 to the power consumption during the calibration test. The N_2 flow rate was maintained at 2 L/min to produce turbulent conditions to prevent heat transfer limitations in the axial direction. A constant heat capacity (C_p) value of 30.93 kJ/k-mol K and ideal gas behavior were assumed for N_2. The calibrated value of η was 0.255 during the experiments. The heat sink capacity (Q) was calculated using Equation (7) assuming that the net power consumption was provided to maintain isothermal conditions against the endothermic reaction heat [47].

4.4. Catalyst Characterization

XRD measurements were carried out on a D/MAX-2500V X-ray diffractometer (Rigaku, Akishima-shi, Tokyo, Japan) with Ni-filtered Cu K_α (λ = 0.154 nm) radiation at 40 kV and 200 mA. The XRD patterns were obtained in continuous scan mode in the 2θ range of 15–90° at 5°/min. The layer

spacings (d) and crystallite sizes (τ) of the catalysts were calculated using the Bragg (Equation (8)) and Scherrer (Equation (9)) equations, respectively, for the (002) crystal face.

$$d_{002} = \frac{\lambda}{2sin\theta_{002}} \tag{8}$$

$$\tau = \frac{K\lambda}{\beta_{002}cos\theta_{002}} \tag{9}$$

Here, λ is the X-ray wavelength, β is the line broadening at half the maximum intensity (FWHM) after subtracting the instrumental line broadening in radians, and θ is the Bragg angle.

SEM images were obtained using a field-emission scanning electron microscope (FESEM S-4700, Hitachi Ltd., Chiyoda-ku, Tokyo, Japan) equipped with an EDX detector. The Brunauer–Emmett–Teller (BET) surface area, pore volume, and average pore diameter were determined using sorption analysis and porosimetry system ASAP2020 (Micromeritics Co., Norcross, GA, USA) based on N_2 physisorption at liquid nitrogen temperature (77 K). The elemental (C, O, N, and Na) compositions of the carbon surfaces were determined by XPS using an AXIS ultra-delay line detector (Kratos Analytical Ltd., Manchester, UK) using monochromatic Al K_α (1486.6 eV) radiation. The XPS spectra were deconvoluted and the atomic compositions were determined after Shirley background subtraction. NH_3-TPD profiles were obtained using Bel-Cat-41 apparatus (MicrotracBel Co., Osaka, Japan). Before analysis, 50 mg of sample was pretreated at 500 °C under He flow for 1 h to remove water and impurities and then, saturated with a gas mixture of 2% NH_3 balanced in He at 50 °C for 30 min. The samples were subsequently treated with pure helium for 30 min to remove physisorbed NH_3 and then, heated under He flow to 750 °C at a rate of 10 °C/min. The chemically desorbed NH_3 profiles were measured using a TCD. The IR spectra for the identification of the functional groups on the catalyst surfaces were acquired using a Nicolet iS50 spectrometer (Thermo Fisher Scientific, Waltham, MA, USA) equipped with a deuterated triglycine sulfate (DTGS) detector. Samples were prepared by mixing 1 mg of the catalyst with 300 mg of KBr. Then, a thin pellet was obtained after compression at 50 MPa. The in situ NH_3 desorption IR spectrum analysis was measured using a DRIFT cell equipped with a mercury cadmium telluride (MCT) detector. Prior to the analysis, 20 mg of catalyst was pretreated to remove impurities and water under N_2 atmosphere at 300 °C. The background spectra were obtained after cooling to 50 °C. Subsequently, the sample was saturated with 2% NH_3 gas mixture and purged with pure N_2 for 30 min. Finally, the spectra were recorded up to 500 °C in intervals of 100 °C.

5. Conclusions

In this study, acid/base-treated activated carbon catalysts were investigated as novel catalysts for low-temperature endothermic supercritical cracking of *n*-dodecane applicable for use in heat management systems in supersonic vehicles. The treatment of AC with base results in the formation of unsaturated sp^3 hybridized carbon atoms acting as Lewis acid sites, whereas acid treatment induces the formation OFGs such as carboxylic (COOH), which act as Brønsted acid sites. Moreover, the sequential base and acid treatment on AC was effective in generating both Brønsted and Lewis acid sites with strong acidity, as well as large ASDs. The liquid fuel conversion and gaseous paraffin (C_1-C_4) yield showed correlation with total ASD. In contrast, the overall gaseous product yield, gaseous olefin (C_1-C_4) yield, and heat sink capacity matched the order of strong ASD. The acid/base-treated AC catalysts showed high activity at 450 °C, and the formation of coke was thermodynamically suppressed, confirming their potential for the development of a heat management system for supersonic vehicles.

Supplementary Materials: The following are available online at http://www.mdpi.com/2073-4344/10/10/1149/s1, Figure S1: Experimental device for the catalytic cracking of n-dodecane, Figure S2. N2 adsorption–desorption isotherms, Figure S3. XRD patterns of the fresh ACs and ZSM-5 zeolite, Figure S4. X-ray photoelectron spectroscopy survey scans of AC catalysts (B.E. = binding energy), Figure S5. Deconvolution of the XPS C1s spectra of the AC catalysts, Figure S6. Gas formation profiles over ACs and ZSM-5 at 450 °C and 4 MPa, Table S1 Energy-dispersive X-ray analysis (EDX) and surface concentration (at%) determined by XPS of the ACs, Table S2 Lattice spacings

(d002) and crystallite sizes (τ) of the ACs, Table S3 Assignments of FT-IR vibration bands in Fig. 5, Table S4 Effects of AC and ZSM-5on the liquid products of n-dodecane cracking as determined by GC-DHA, Table S5 Catalytic performance of supercritical catalytic cracking of n-dodecane in the references, Table S6 GC conditions for liquid product analysis, Table S7 GC conditions for gaseous product analysis.

Author Contributions: K.H.S. (methodology, data curation, writing original draft preparation, formal analysis), S.K.J. (supervision, investigation, funding acquisition), B.H.J. (supervision, investigation, funding acquisition), K.-Y.L. (supervision), and H.J.K. (Conceptualization, writing, reviewing, and editing, project administration). All authors have read and agreed to the published version of the manuscript.

Funding: This research was funded by the Grant-in-aid from the Korean Agency for Defense Development (ADD) funded by the Korean Defense Acquisition Program Administration (DAPA) and the Korean Ministry of National Defense (MND).

Acknowledgments: The authors would like to thank Editage (http://www.editage.com) for editing and reviewing this manuscript for English language.

Conflicts of Interest: The authors declare no conflict of interest.

References

1. Edwards, T. Liquid fuels and propellants for aerospace propulsion: 1903–2003. *J. Propuls. Power* **2003**, *19*, 1089–1107. [CrossRef]
2. Kay, I.W.; Peschke, W.T.; Guile, R.N. Hydrocarbon-fueled scramjet combustor investigation. *J. Propuls. Power* **1992**, *8*, 507–512. [CrossRef]
3. Edwards, T. Cracking and deposition behavior of supercritical hydrocarbon aviation fuels. *Combust. Sci. Technol.* **2006**, *178*, 307–334. [CrossRef]
4. Edwards, T. Advancements in gas turbine fuels from 1943 to 2005. *J. Eng. Gas Turbines Power* **2007**, *129*, 13–20. [CrossRef]
5. Puri, P.; Ma, F.; Choi, J.Y.; Yang, V. Ignition characteristics of cracked JP-7 fuel. *Combust. Flame* **2005**, *142*, 454–457. [CrossRef]
6. Ritchie, A.W.; Nixon, A.C. Dehydrogenation of Methylcyclohexane over a Platinum-Alumina Catalyst in Absence of Added Hydrogen. *Ind. Eng. Chem. Prod. Res. Dev.* **1966**, *5*, 59–64. [CrossRef]
7. Jiao, Y.; Liu, A.; Li, C.; Wang, J.; Zhu, Q.; Li, X.; Chena, Y. Catalytic cracking of RP-3 jet fuel over wall-coated Pt/ZrO2-TiO2-Al2O3 catalysts with different Al2O3 ratios. *J. Anal. Appl. Pyrolysis* **2015**, *111*, 100–107. [CrossRef]
8. Xian, X.; Liu, G.; Zhang, X.; Wang, L.; Mi, Z. Catalytic cracking of n-dodecane over HZSM-5 zeolite under supercritical conditions: Experiments and kinetics. *Chem. Eng. Sci.* **2010**, *65*, 5588–5604. [CrossRef]
9. Lee, S.; Lee, S.; Kumbhalkar, M.D.; Wiaderek, K.M.; Dumesic, J.; Winans, R.E. Effect of Particle Size upon Pt/SiO2 Catalytic Cracking of n-Dodecane under Supercritical Conditions: In situ SAXS and XANES Studies. *ChemCatChem* **2017**, *9*, 99–102. [CrossRef]
10. Ji, Y.; Yang, H.; Yan, W. Effect of alkali metal cations modification on the acid/basic properties and catalytic activity of ZSM-5 in cracking of supercritical n-dodecane. *Fuel* **2019**, *243*, 155–161. [CrossRef]
11. Li, S.; Wang, Z.; Zhang, H.; Liu, Z.; Wang, J.; Zhu, Q.; Li, X.; Chen, Y. The effects of MxOy (M = K, Ba, and Sr) promoters on inhibiting carbon deposit during catalytic cracking reactions. *J. Anal. Appl. Pyrolysis* **2017**, *123*, 269–277. [CrossRef]
12. Liu, B.; Wang, Z.; Zhu, Q.; Li, X.; Wang, J. Performance of Pt/ZrO2–TiO2–Al2O3 and coke deposition during methylcyclohexane catalytic cracking. *Fuel* **2017**, *200*, 387–394. [CrossRef]
13. Rownaghi, A.A.; Rezaei, F.; Hedlund, J. Selective formation of light olefin by n-hexane cracking over HZSM-5: Influence of crystal size and acid sites of nano- and micrometer-sized crystals. *Chem. Eng. J.* **2012**, *191*, 528–533. [CrossRef]
14. Viswanadham, N.; Kamble, R.; Singh, M.; Kumar, M.; Murali Dhar, G. Catalytic properties of nano-sized ZSM-5 aggregates. *Catal. Today* **2009**, *141*, 182–186. [CrossRef]
15. Ji, Y.; Yang, H.; Yan, W. Strategies to enhance the catalytic performance of ZSM-5 zeolite in hydrocarbon cracking: A review. *Catalysts* **2017**, *7*, 367. [CrossRef]
16. Li, X.; Zhang, H.; Liu, B.; Zhu, Q.; Wang, J.; Li, X. Mo-promoted catalysts for supercritical n-decane cracking. *Appl. Therm. Eng.* **2016**, *102*, 1238–1240. [CrossRef]

17. Jentoft, F.C.; Gates, B.C. Solid-acid-catalyzed alkane cracking mechanisms: Evidence from reactions of small probe molecules. *Top. Catal.* **1997**, *4*, 1–13. [CrossRef]
18. Wojciechowski, B.W. The Reaction Mechanism of Catalytic Cracking: Quantifying Activity, Selectivity, and Catalyst Decay. *Catal. Rev.* **1998**, *40*, 209–328. [CrossRef]
19. Gumming, K.A.; Wojciechowski, B.W. Hydrogen transfer, coke formation, and catalyst decay and their role in the chain mechanism of catalytic cracking. *Catal. Rev.-Sci. Eng.* **1996**, *38*, 101–157. [CrossRef]
20. Boronat, M.; Corma, A. Are carbenium and carbonium ions reaction intermediates in zeolite-catalyzed reactions? *Appl. Catal. A Gen.* **2008**, *336*, 2–10. [CrossRef]
21. Kissin, Y.V. Chemical Mechanisms of Catalytic Cracking over Solid Acidic Catalysts: Alkanes and Alkenes. *Catal. Rev.-Sci. Eng.* **2001**, *43*, 85–146. [CrossRef]
22. Liu, C.; Gao, X.; Zhang, Z.; Zhang, H.; Sun, S.; Deng, Y. Surface modification of zeolite Y and mechanism for reducing naphtha olefin formation in catalytic cracking reaction. *Appl. Catal. A Gen.* **2004**, *264*, 225–228. [CrossRef]
23. Abbot, J. Role of Brønsted and Lewis acid sites during cracking reactions of alkanes. *Appl. Catal.* **1989**, *47*, 33–44. [CrossRef]
24. Park, S.J.; Kim, B.J. Ammonia removal of activated carbon fibers produced by oxyfluorination. *J. Colloid Interface Sci.* **2005**, *291*, 597–599. [CrossRef] [PubMed]
25. Kim, B.J.; Park, S.J. Effects of carbonyl group formation on ammonia adsorption of porous carbon surfaces. *J. Colloid Interf. Sci.* **2007**, *311*, 311–314. [CrossRef] [PubMed]
26. Dos Santos, P.R.; Daniel, L.A. A review: Organic matter and ammonia removal by biological activated carbon filtration for water and wastewater treatment. *Int. J. Environ. Sci. Technol.* **2020**, *17*, 591–606. [CrossRef]
27. Bansal, R.C.; Goyal, M. Adsorptive removal of organic from water, activated carbon adsorption. In *Activated Carbon Adsorption and Environment*; Taylor: Boca Raton, FL, USA, 2005; pp. 297–372.
28. Park, S.J.; Jin, S.Y. Effect of ozone treatment on ammonia removal of activated carbons. *J. Colloid Interface Sci.* **2005**, *286*, 417–419. [CrossRef]
29. Park, S.J.; Kim, Y.M. Influence of anodic treatment on heavy metal ion removal by activated carbon fibers. *J. Colloid Interf. Sci.* **2004**, *278*, 276–281. [CrossRef]
30. Le Leuch, L.M.; Bandosz, T.J. The role of water and surface acidity on the reactive adsorption of ammonia on modified activated carbons. *Carbon N. Y.* **2007**, *45*, 568–578. [CrossRef]
31. Zawadzki, J.; Wiśniewski, M. In situ characterization of interaction of ammonia with carbon surface in oxygen atmosphere. *Carbon N. Y.* **2003**, *41*, 2257–2267. [CrossRef]
32. Kim, J.H.; Hwang, S.Y.; Park, J.E.; Lee, G.B.; Kim, H.; Kim, S.; Hong, B.U. Impact of the oxygen functional group of nitric acid-treated activated carbon on KOH activation reaction. *Carbon Lett.* **2019**, *29*, 281–287. [CrossRef]
33. Datsyuk, V.; Kalyva, M.; Papagelis, K.; Parthenios, J.; Tasis, D.; Siokou, A.; Kallitsis, I.; Galiotis, C. Chemical oxidation of multiwalled carbon nanotubes. *Carbon N. Y.* **2008**, *46*, 833–840. [CrossRef]
34. Liu, Y.; Hu, Z.; Xu, K.; Zheng, X.; Gao, Q. Surface Modification and Performance of Activated Carbon Electrode Material. *Acta Phys.-Chim. Sin.* **2008**, *24*, 1143–1148. [CrossRef]
35. Chingombe, P.; Saha, B.; Wakeman, R.J. Surface modification and characterisation of a coal-based activated carbon. *Carbon N. Y.* **2005**, *43*, 3132–3143. [CrossRef]
36. Vinke, P.; van der Eijk, M.; Verbree, M.; Voskamp, A.F.; van Bekkum, H. Modification of the surfaces of a gasactivated carbon and a chemically activated carbon with nitric acid, hypochlorite, and ammonia. *Carbon N. Y.* **1994**, *32*, 675–686. [CrossRef]
37. March, J. *Advanced Organic Chemistry*, 3rd ed.; John Wiley & Sons: New York, NY, USA, 1985; p. 1072.
38. Ogata, Y. *Oxidation in Organic Chemistry*; Academic Press: New York, NY, USA, 1978; Volume SC, p. 295.
39. Raymundo-Piñero, E.; Azaïs, P.; Cacciaguerra, T.; Cazorla-Amorós, D.; Linares-Solano, A.; Béguin, F. KOH and NaOH activation mechanisms of multiwalled carbon nanotubes with different structural organisation. *Carbon N. Y.* **2005**, *43*, 786–795. [CrossRef]
40. Islam, M.A.; Ahmed, M.J.; Khanday, W.A.; Asif, M.; Hameed, B.H. Mesoporous activated carbon prepared from NaOH activation of rattan (Lacosperma secundiflorum) hydrochar for methylene blue removal. *Ecotoxicol. Environ. Saf.* **2017**, *138*, 279–285. [CrossRef]
41. Ramesh, T.; Rajalakshmi, N.; Dhathathreyan, K.S. Synthesis and characterization of activated carbon from jute fibers for hydrogen storage. *Renew. Energy Environ. Sustain.* **2017**, *2*, 4. [CrossRef]

42. Shim, J.W.; Park, S.J.; Ryu, S.K. Effect of modification with HNO_3 and NaOH on metal adsorption by pitch-based activated carbon fibers. *Carbon N. Y.* **2001**, *39*, 1635–1642. [CrossRef]
43. Nian, Y.R.; Teng, H. Influence of surface oxides on the impedance behavior of carbon-based electrochemical capacitors. *J. Electroanal. Chem.* **2003**, *540*, 119–127. [CrossRef]
44. Chiang, Y.C.; Lin, W.H.; Chang, Y.C. The influence of treatment duration on multi-walled carbon nanotubes functionalized by H 2 SO 4 /HNO 3 oxidation. *Appl. Surf. Sci.* **2011**, *257*, 2401–2410. [CrossRef]
45. Beamson, G.; Briggs, D. High resolution XPS of organic polymers, the scienta ESCA A300 database, Wiley, Chichester 1992. *Adv. Mater.* **1993**, *5*, 778.
46. De La Puente, G.; Pis, J.J.; Menéndez, J.A.; Grange, P. Thermal stability of oxygenated functions in activated carbons. *J. Anal. Appl. Pyrolysis* **1997**, *43*, 125–138. [CrossRef]
47. Song, K.H.; Jeong, S.K.; Park, K.T.; Lee, K.Y.; Kim, H.J. Supercritical catalytic cracking of n-dodecane over air-oxidized activated charcoal. *Fuel* **2020**, *276*, 118010. [CrossRef]
48. Biniak, S.; Szymański, G.; Siedlewski, J.; Światkoski, A. The characterization of activated carbons with oxygen and nitrogen surface groups. *Carbon N. Y.* **1997**, *35*, 1799–1810. [CrossRef]
49. Lambert, J.B.; Shurvell, F.H.; Lightner, D.A.; Cooks, R.G. *Organic Structural Spectroscopy*; Prentice Hall: Upper Saddle River, NJ, USA, 1998.
50. Vasu, A.E. Surface modification of activated carbon for enhancement of nickel(II) adsorption. *E-J. Chem.* **2008**, *5*, 814–819. [CrossRef]
51. Fanning, P.E.; Vannice, M.A. A DRIFTS study of the formation of surface groups on carbon by oxidation. *Carbon N. Y.* **1993**, *31*, 721–730. [CrossRef]
52. Park, S.H.; McClain, S.; Tian, Z.R.; Suib, S.L.; Karwacki, C. Surface and Bulk Measurements of Metals Deposited on Activated Carbon. *Chem. Mater.* **1997**, *9*, 176–183. [CrossRef]
53. Zawadzki, J. *Spektroskopia W Podczerwieni Zjawisk Powierzchniowych na Weglach (Infrared Spectroscopy of the Surface Phenomena on Carbons)*; UMK: Toruń, Poland, 1980.
54. Socrates, G. *Infrared Characteristic Group Frequencies*; Wiley: Chichester, UK, 1994.
55. Solum, M.S.; Pugmire, R.J.; Jagtoyen, M.; Derbyshire, F. Evolution of carbon structure in chemically activated wood. *Carbon N. Y.* **1995**, *33*, 1247–1254. [CrossRef]
56. Barthos, R.; Lónyi, F.; Onyestyák, G.; Valyon, J. IR, FR, and TPD study on the acidity of H-ZSM-5, sulfated zirconia, and sulfated zirconia-titania using ammonia as the probe molecule. *J. Phys. Chem. B* **2000**, *104*, 7311–7319. [CrossRef]
57. Shu, Y.; Sun, H.; Quan, X.; Chen, S. Enhancement of catalytic activity over the iron-modified Ce/TiO2 catalyst for selective catalytic reduction of NOx with ammonia. *J. Phys. Chem. C* **2012**, *116*, 25319–25327. [CrossRef]
58. Gonçalves, M.; Sánchez-García, L.; Oliveira Jardim, E.; De Silvestre-Albero, J.; Rodríguez-Reinoso, F. Ammonia removal using activated carbons: Effect of the surface chemistry in dry and moist conditions. *Environ. Sci. Technol.* **2011**, *45*, 10605–10610. [CrossRef] [PubMed]
59. Serp, P.; Machado, B. *Nanostructured Carbon Materials for Catalysis*; Royal Society of Chemistry: London, UK, 2015; ISBN 978-1-84973-909-2.
60. Seo, M.G.; Kim, S.; Lee, D.W.; Jeong, H.E.; Lee, K.Y. Core-shell structured, nano-Pd-embedded SiO_2-Al_2O_3 catalyst (Pd@SiO_2-Al_2O_3) for direct hydrogen peroxide synthesis from hydrogen and oxygen. *Appl. Catal. A Gen.* **2016**, *511*, 87–94. [CrossRef]
61. Guisnet, M.; Magnoux, P. Organic chemistry of coke formation. *Appl. Catal. A Gen.* **2001**, *212*, 83–96. [CrossRef]
62. *ASTM D6730-01*; ASTM International: West Conshohocken, PA, USA, 2011.